

Electronic Supplemental Material for:

**Solvent-induced ion clusters generate long-ranged double-layer forces
at high ionic strengths**

David Ribar*, Clifford E. Woodward**, and Jan Forsman*

*Computational Chemistry, Lund University

P.O.Box 124, S-221 00 Lund, Sweden

**School of Physical, Environmental and Mathematical Sciences

University College, University of New South Wales, ADFA

Canberra ACT 2600, Australia

Contents

Simulation and model details	2
Testing effects with a varying ε_c	4
Effects of “wall softness”	4
Size dependence at a constant slit separation	6
Structural analyses	7
Configurational snapshots of sRPM(ϕ_n) systems	7
Species resolved pair correlations for sRPM(ϕ_n)	11
Charge-charge and density-density correlations for sRPM(ϕ_n)	13
Structural comparison, using different sPMF:s in a concentrated bulk solution	23
References	23

SIMULATION AND MODEL DETAILS

Herein, we provide a more detailed description of our model system, and how the simulations were conducted. In order to make the Electronic Supplemental Information (ESI) self-contained, there are some inevitable repetitions from the more condensed description in the main manuscript. The two surfaces carried a uniform (smeared-out) surface charge density, $\sigma_s = 1/70 \approx -0.014336 e/\text{\AA}^2$, which is a value typical to mica [1], i.e. the surfaces used in SFA experiments. The surfaces were located at $z = 0$ and $z = H$. They were parallel and flat, extending infinitely in the (x, y) plane utilising periodic boundary conditions. Equilibrium between the simulated salt solution, located between these walls, and the bulk salt solution, was ensured via grand canonical moves, with a prescribed chemical potential (that defines the bulk concentration). The simulation box had an extension along the x axis, such that $-L/2 < x < L/2$, with an identical extension along y , with $L = 160 \text{\AA}$. The standard ‘‘charged sheet’’ method [2] with the minimum image convention was utilised to account for long-ranged interactions, which were previously shown to excellently reproduce the structure of concentrated electrolyte solutions at high concentrations [3]. Cluster moves were implemented for both systems, leading to crucial improvements of the statistical performance.

The initial number of cations and anions were chosen such that the net ion charge neutralises the total wall charge. The initial configuration was a random configurational realisation of hard spheres with an identical diameter, to ensure no hard-sphere overlap. After the short initialization simulation, the electrostatics were ‘turned on’. For each subsequent simulation, the final configuration was taken as the starting configuration. The grand canonical deletions and insertions then involved a cation as well as an anion, ensuring that electroneutrality was retained [4]. The interaction energy $\phi_{ij}(r)$ between ions i and j of equal diameter d , with valencies Z_i and Z_j , separated a distance r , was given by

$$\beta\phi_{ij}(r) = \begin{cases} \infty; & r \leq d \\ l_B(\text{bulk}) \frac{Z_i Z_j}{r} + \beta\phi_\alpha(r); & r > d \end{cases} \quad (1)$$

where $\alpha = w$ or n , depending on the choice of sPMF, described in detail in the main article, and $l_B(\text{bulk}) = \beta e_0^2 / (4\pi\epsilon_0\epsilon_b)$. All simulations were performed at 298 K.

Equilibrations required 10^9 attempted configurations, starting from a random distribution, as described above. The number of attempted configurations used for pressure sampling varied with separation, as larger separations in practise require a higher accuracy, given the small difference to the bulk pressure. At separations above 50\AA , we devoted more than 10^{11} configurations to pressure sampling, at each investigated separation.

In order to improve force statistics, the confining walls were modelled as softly repulsive, rather than completely hard. Specifically, an ion located a transverse distance δ from a wall experienced a non-electrostatic truncated and shifted wall potential, $W_{\text{soft}}(\delta)$:

$$\beta W_{\text{soft}}(\delta) = \begin{cases} 0; & \delta \geq \delta_C \\ A_w \left[\left(\frac{d}{\delta}\right)^4 - \left(\frac{d}{\delta_C}\right)^4 \right]; & \delta < \delta_C \end{cases}, \quad (2)$$

where β is the inverse thermal energy. The amplitude A_w was set equal to 5 for our reference ion diameter $d = 3 \text{\AA}$. We have also explored a model with $d = 4 \text{\AA}$, in which case A_w was modified to ensure the same soft wall repulsion, i.e. $A_w(d = 4 \text{\AA}) = 5(3/4)^4$. The soft wall potential was truncated at $\delta_C = 12 \text{\AA}$. The parameters defining the potential were obviously chosen in a rather *ad hoc* manner, but on the other hand, the surface interactions are insensitive to the repulsive part of the wall potential, as we will demonstrate below.

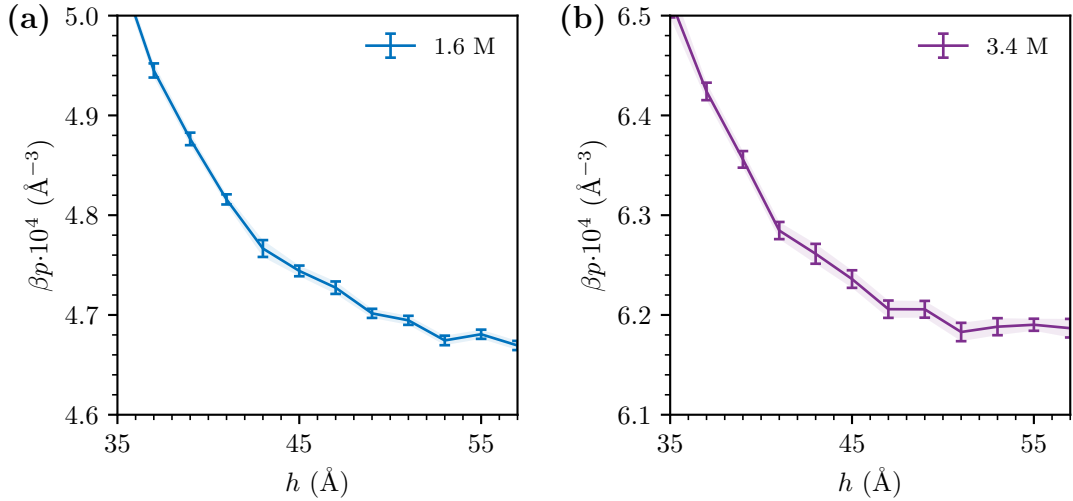


FIG. 1: Longest range osmotic pressure data for (a) the 1.6 M system, and (b) the 3.4 M system, using ϕ_n as the chosen sPMF. The error bars denote \pm one standard deviation.

The (osmotic) pressure, $p(H)$, acting transverse to the walls was evaluated from the average normal force across the walls. Bulk salt concentrations and pressures, p_b , were evaluated at large distances with neutral walls, for each given choice of salt chemical potential. The net osmotic pressure, p_{net} then evaluated as $p_{net}(H) = p(H) - p_b$. The corresponding free energy per unit area, $g_s(H)$, can in principle be obtained by integration: $g_s(H) = \int_H^\infty p_{net}(H')dH'$, and using the Derjaguin Approximation, we obtain an estimate of the expected force per radius, F/R , that is measured by the Surface Force Apparatus, SFA: $F/R \approx 2\pi g_s$. However, we were not able to achieve satisfactory statistics at very large separations, so in practice, we made cubic spline fits of the net pressure up to $H = 60 \text{ \AA}$, which then were integrated. Since the fringes from which “separation” is measured by the SFA, are expected to reflect the distance between planes of refractive index shifts, it makes sense to measure surface separation as $h \equiv H - d$. Moreover, given our lack of the “tail pressure” contribution to the free energy integral, we permitted a small shift to our predicted F/R curves, so that they approximately coincided with SFA data (for a concentration of 2 M) at $H = 60 \text{ \AA}$ i.e. $h = 60 \text{ \AA} - d$.

To showcase the longest range pressure statistics, Figure 1 presents the osmotic pressure obtained from simulations, with the error bars depicting the standard deviations. Note the difference in scale, since the bulk osmotic pressure was not removed, i.e. we present the raw unmodified pressure data.

TESTING EFFECTS WITH A VARYING ϵ_c

Our model is based on the assumption that local dielectric saturation effects do not change with the salt concentration. However, as we also discuss in the main paper, the mechanisms that we attempt to account for with our coarse-grained description are in reality quite complex. One could easily envisage that many-body interactions, which mainly become relevant at high concentrations and in the presence of clusters, will lead to more pronounced dielectric saturation effects. In our model description, this could crudely be accounted for by allowing a gradual drop of ϵ_c , as the salt concentrations increase. We have established that with $d = 3 \text{ \AA}$, we will observe global flocculation at about 3.45 M, if ϵ_c drops slightly below 23. Hence, one can argue that $\epsilon_c = 23$ should be regarded as a high concentration lower limit, and consider higher values at low salt concentrations. A drawback is of course that this will require additional assumptions, and effectively a new parameter (the concentration dependence of ϵ_c). It is nevertheless of interest

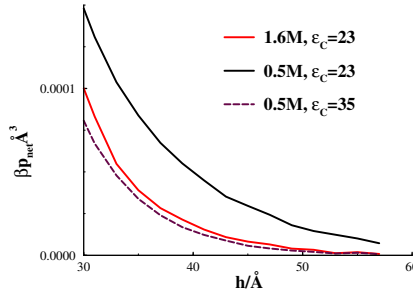


FIG. 2: Simulated net pressures, with $d = 3 \text{ \AA}$, at two different salt concentrations: 0.5M and 1.6M. In the former case, the pressure curve with an increased value of ϵ_c (compared to the reference: 23) is also included.

to briefly investigate how the results might change if we were to implement such an extension of the sRPM(ϕ_n). In Figure 2, we note that an increase of ϵ_c from its reference value of 23, at 1.6 M, to 35 at 0.5 M, will see the latter interactions more short-ranged than the former. This is in qualitative agreement with *anomalous underscreening*, with surface forces becoming more long-ranged as the ionic strength increases, beyond some threshold value.

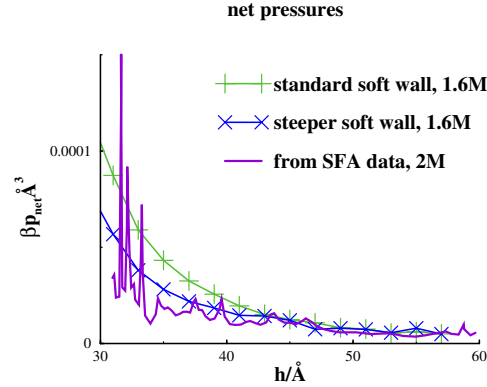
EFFECTS OF “WALL SOFTNESS”

In the main paper, we modelled the non-electrostatic ion-wall interaction by a soft repulsion, decaying as δ^{-4} , where delta is the transverse distance between the ion and the wall. It was truncated and shifted at $\delta_c = 12 \text{ \AA}$, but one could still argue that it is a bit unrealistically soft, given that it essentially represents exchange repulsions. The advantage is better pressure statistics, at least compared with the hard wall option. Here, we will evaluate effects from this choice by comparing with a steeper, albeit still soft option. We will specifically investigate

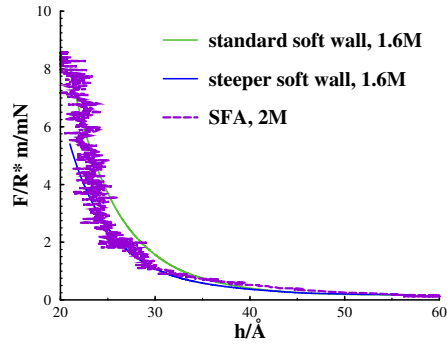
interactions at 1.6 M, with $d = 3 \text{ \AA}$, with an alternative ion-wall potential, W_{steep} :

$$\beta W_{steep}(\delta) = \begin{cases} 0; & \delta \geq \delta_C \\ A_w \left[\left(\frac{d}{\delta}\right)^6 - \left(\frac{d}{\delta_C}\right)^6 \right]; & \delta < \delta_C \end{cases} \quad (3)$$

where (again) $A_w = 5$ and $\delta_c = 6 \text{ \AA}$. We have only investigated systems in which $d = 3 \text{ \AA}$, with this wall potential. The comparison is shown in Figure 3. We note that the functional form



(a)



(b)

FIG. 3: Comparisons of results obtained with wall potentials W_{soft} (“soft”), and W_{steep} (“steep”), at high salt concentration, with $d = 3 \text{ \AA}$. Raw SFA data (from ref. [5]) were kindly send to us by prof. Susan Perkin. Simulated curves have been shifted, to agree with SFA data at the largest investigated separation.

(a) Net pressures. Also shown is the “soft” wall pressure curve, with a separation displacement by -3 \AA .

(b) Force on radius curves (crossed cylinders).

of the interactions seems to be almost identical, but that the steeper wall potential generates a separation shift of the interaction curves by about 2-3 \AA .

SIZE DEPENDENCE AT A CONSTANT SLIT SEPARATION

To probe the size dependence of the formed clusters with the "narrow" sRPM, ϕ_n , we computed the ion cluster probabilities for systems at a constant $H = 24 \text{ \AA}$ and $L = 160 \text{ \AA}$ and $L = 270 \text{ \AA}$. For completeness, the cluster analysis methodology is repeated here. P_c measures the probability for a cluster of size N_c . A cluster is defined such that an ion must be within a distance δ_c or less, of at least one other ion within a cluster, in order to be a member of that cluster. We have set $\delta_c = d + 2\text{\AA}$. These distributions were obtained from grand canonical slit simulations, where the chemical potential is adjusted so that the corresponding bulk solution has a concentration of about 1.8 M. The distributions are based on at least 50 different configurations, separated by 10^8 attempted moves to ensure statistical independence.

As can be seen on Figure 4, we can observe that the size of the periodic box L has no significant effect on the cluster distribution, besides the expected improvement of the statistics for larger systems.

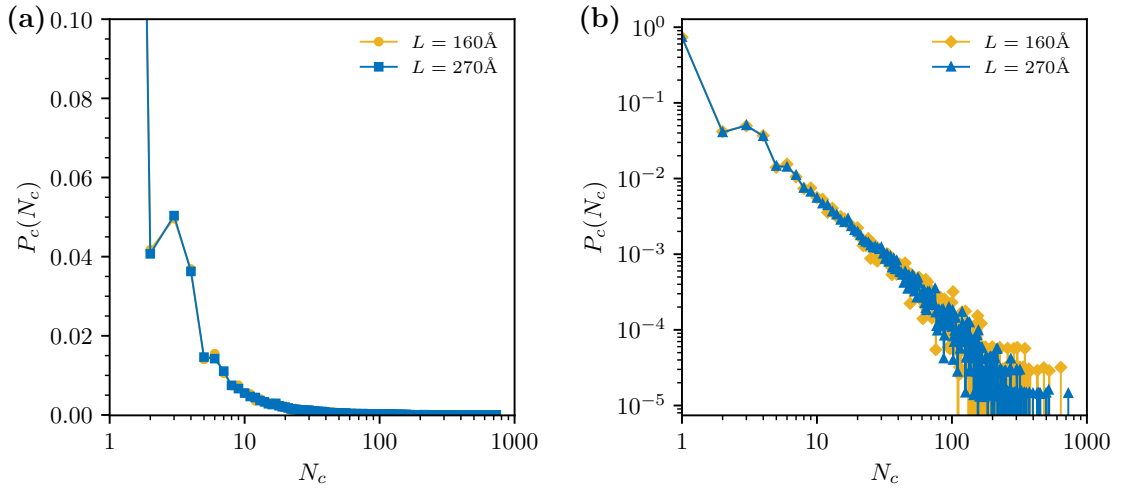


FIG. 4: Cluster size analysis of a 1.8 M ϕ_n sRPM system at $H = 24 \text{ \AA}$ and two lengths of the periodic box. (a) Linear scale and (b) logarithmic scale.

STRUCTURAL ANALYSES

Configurational snapshots of sRPM(ϕ_n) systems

In order to explicitly present the clusters that form within the confining slit, we include Figure 5 of the sRPM(ϕ_n) system at $c \approx 3.4$ M. We can observe clusters of various sizes within the simulation box. The first three rows are all systems in negatively charged surfaces, hence the higher density of cations (in blue) at the surface edges. The last row presents the reference neutral walls system.

Figure 6 presents snapshots for a $c \approx 1.8$ M system, and Figure 7 for the lowest concentration studied at $c \approx 0.13$ M.

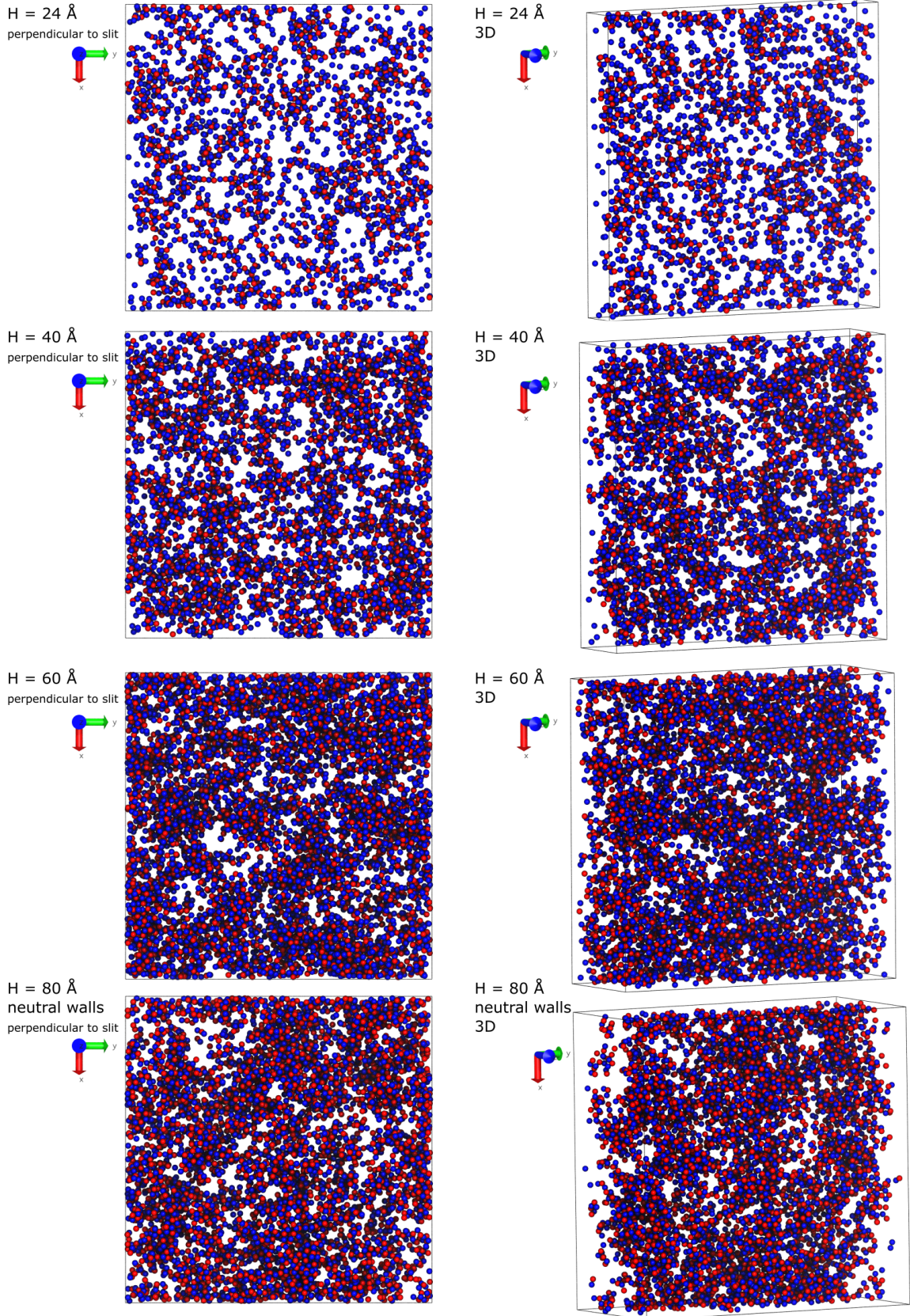


FIG. 5: Final configurational snapshots from simulations of sRPM(ϕ_n) systems at $c \approx 3.4 \text{ M}$ in the slit. Presented are $H \in \{24, 40, 60, 80\} \text{ \AA}$ systems, with $H = 80 \text{ \AA}$ denoting the neutral wall system. Blue denotes the cations and red the anions. The first column presents the system perpendicular to the confining slit, while the second presents the system at an angle.

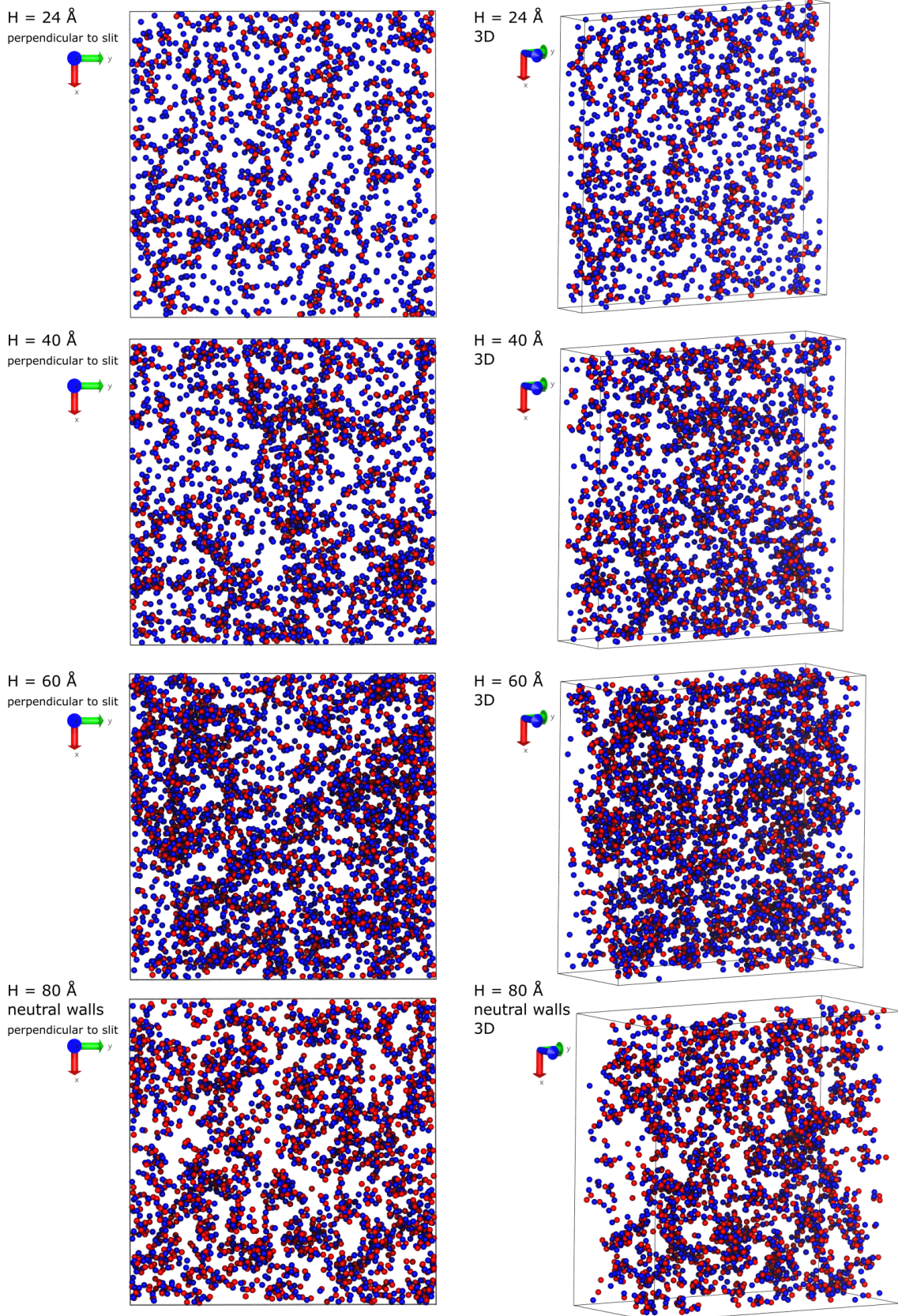


FIG. 6: Final configurational snapshots from simulations of sRPM(ϕ_n) systems at $c \approx 1.8 \text{ M}$ in the slit. Presented are $H \in \{24, 40, 60, 80\} \text{ \AA}$ systems, with $H = 80 \text{ \AA}$ denoting the neutral wall system. Blue denotes the cations and red the anions. The first column presents the system perpendicular to the confining slit, while the second presents the system at an angle.

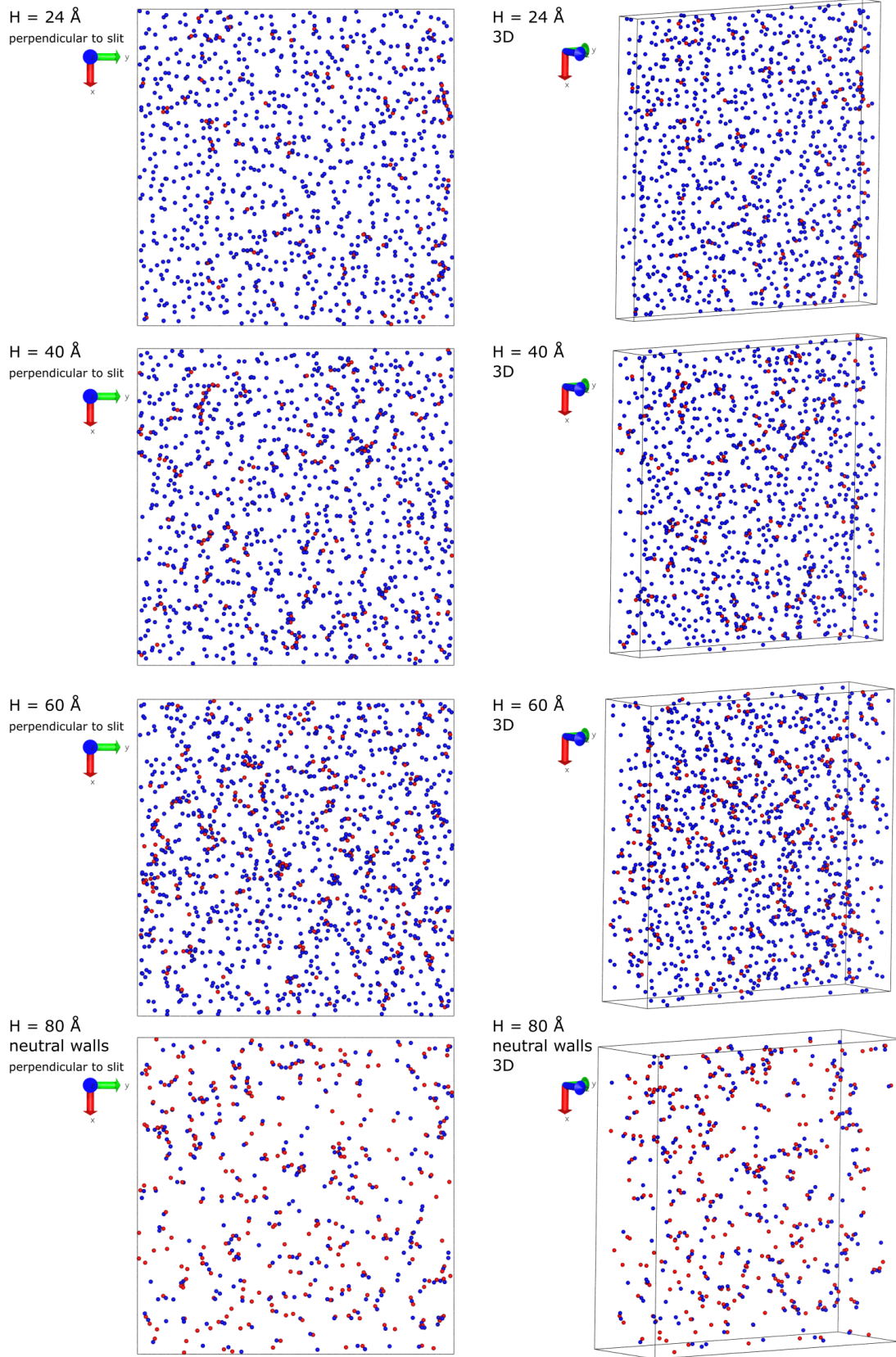


FIG. 7: Final configurational snapshots from simulations of sRPM(ϕ_n) systems at $c \approx 0.13 M$ in the slit. Presented are $H \in \{24, 40, 60, 80\} \text{ \AA}$ systems, with $H = 80 \text{ \AA}$ denoting the neutral wall system. Blue denotes the cations and red the anions. The first column presents the system perpendicular to the confining slit, while the second presents the system at an angle.

Species resolved pair correlations for sRPM(ϕ_n)

In order to explore the structure of the sRPM(ϕ_n) electrolytes confined in charged slits at different slit widths, we investigated two extreme concentration cases of the $d = 3 \text{ \AA}$ system. We have chosen a lower concentration $c \approx 0.13 \text{ M}$, and the highest concentration case $c \approx 3.4 \text{ M}$ used in this study. The equilibrated number densities along the z coordinate, $n(z)$, are presented on Figure 8. We can observe how the difference in number densities at the mid-plane changes as we increase the slit width, presented on the right most plots. Of interest is the fact that the $\Delta n(z)$ becomes small yet never 0 in both cases (for the 3.4 M case, the $\Delta n(z) \approx 0.02 \text{ M}$ at $H = 60 \text{ \AA}$).

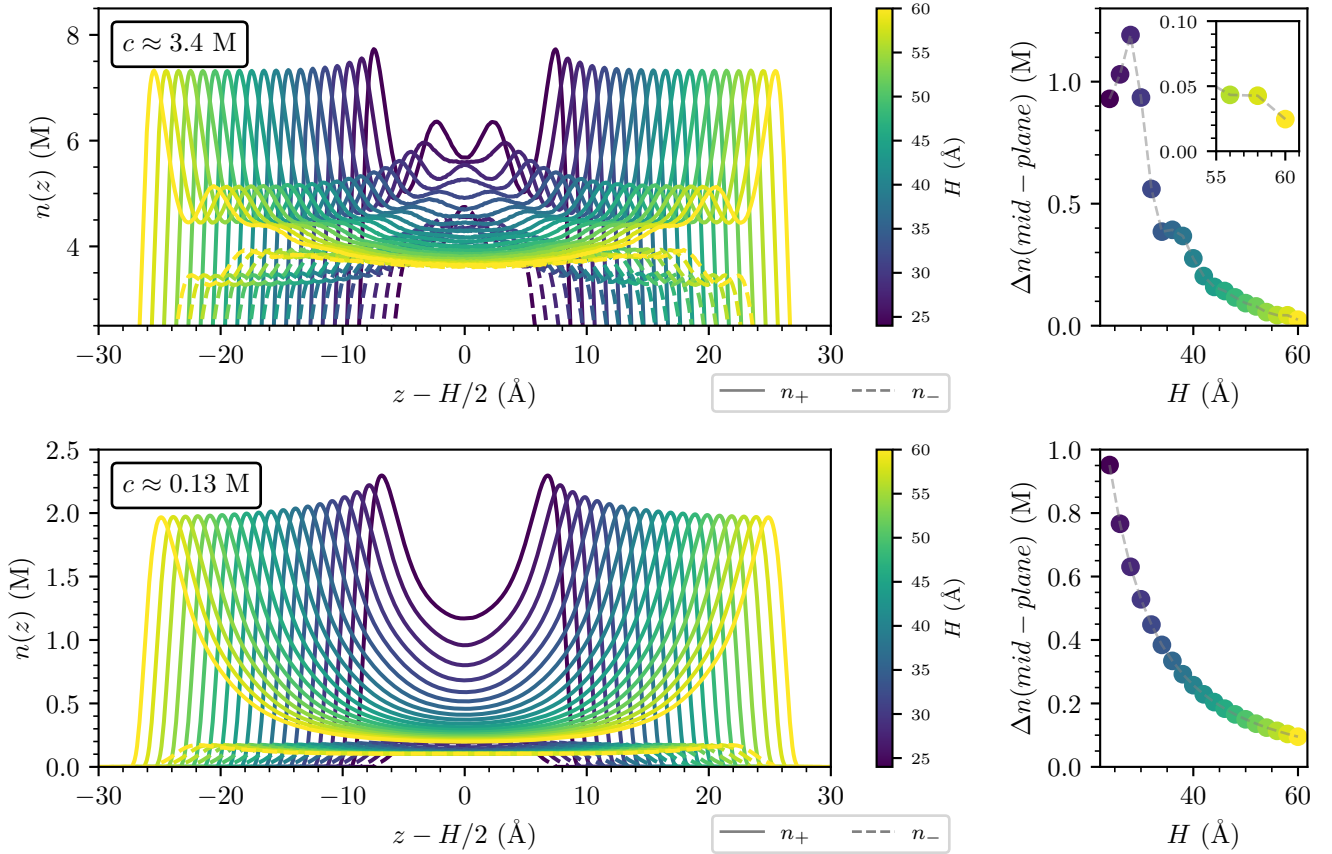


FIG. 8: The first column presents the $n(z)$ number density distributions for the higher concentration $\approx 3.4 \text{ M}$ (top), and $\approx 0.13 \text{ M}$ system (bottom). The colour of the lines denotes the slit width used. The second column presents the difference $\Delta n(z) = n_+(z) - n_-(z)$ for z at the mid-plane.

To obtain structural information of the fluid parallel to the slit, we computed $2D$ species resolved pair correlation functions, $g_{\mu\nu}(\rho)$, for selected small sampling areas in the transverse z direction. The process is schematically presented on Figure 9. We selected two sampling positions the size of one particle diameter, one at the mid-plane, and the second at both walls. The wall sampling area was chosen so that the soft wall potential reaches a maximum of $k_B T$

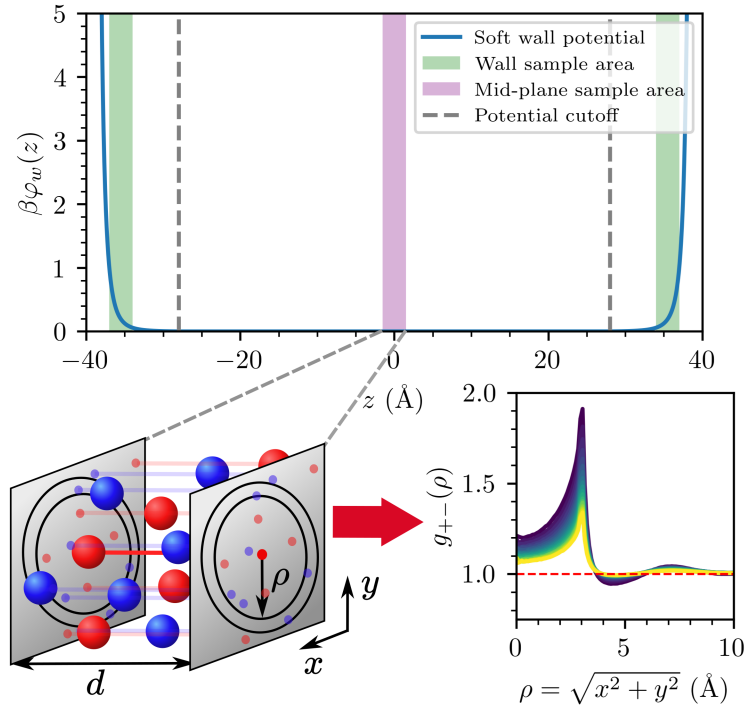


FIG. 9: Schematic presentation of the $g_{\mu\nu}(\rho)$ procedure, with the top figure presenting the soft wall potential at a slit width of 80 \AA . The shaded areas present the sampling widths of one particle diameter d , both at the walls and the mid-plane. In each sample width, the z particle coordinate is disregarded, thereby projecting the contents of the 3D slit onto a 2D plane, visualised on the bottom left figure. $\rho = \sqrt{x^2 + y^2}$ values are calculated in order to produce 2D pair correlation functions, $g_{\mu\nu}(\rho)$, presented on the bottom right figure.

energy units within this area, to improve the sampling statistics. In each sampling iteration the z coordinate of particles was disregarded, followed by a histogram count of radial distances, $\rho = \sqrt{x^2 + y^2}$. Periodic boundary conditions were utilized in the (x, y) directions. The distance histograms were normalised to remove volume (or in this case area) effects, and normalised to 1 by dividing the final correlation function with an average values from 60 to 80 \AA .

The 2D pair correlation functions, $g_{\mu\nu}(\rho)$, were computed at the respective ρ values for $\mu\nu \in \{++, +-, --\}$ correlations. We also computed the total correlation functions via $h_{\mu\nu}(\rho) = g_{\mu\nu}(\rho) - 1$ to produce asymptotic analysis plots via $\rho|h_{\mu\nu}(\rho)|$, in order to investigate the asymptotic behaviour of the fluid parallel to the charged slit.

Figures 10 and 11 present the results for the $c \approx 3.4$ M case, and Figures 12 and 13 for the lower concentration case, $c \approx 0.13$ M. The first column presents the pair correlation functions, with inserts showing a zoomed-in plot extending to the farthest ρ . The second column presents the asymptotic analysis for the pair correlation functions. On Figure 10, presenting the results obtained at the mid plane, we can see that increasing the slit width (colour ranging from an initial purple to a final yellow) gradually lessens the oscillatory behaviour and introduces a long ranging exponential slope. Of importance is the fact that the oscillations decay below statistical uncertainty for values below $\rho_{max} = L/2 = 80$ \AA . This implies that the system is not

exhibiting behaviour characteristic of frozen systems (with oscillations persisting throughout the whole range of ρ). The asymptotic analysis demonstrates the gradual shift from a dampened oscillatory behaviour at the longest range, to a simple exponential decay dictated by the density structural correlations, as discussed in our recent publication [6]. At the largest wall separations, we can observe $g_{++}(\rho) \approx g_{+-}(\rho)$ where both correlation functions approach unity from above, exactly as described in [6], again due to density correlations, originating from cluster-cluster interactions, dominating the asymptotic behaviour of the system. Figure 11 presents the same high concentration system sampled at the walls. We observe similar behaviour as compared with Figure 10, albeit with less pronounced oscillations. Importantly, the system does not exhibit frozen characteristic even at the walls of the charged slit. We can however observe the difference between the neutral and charged wall correlations, as the dashed line deviates more for the wall case as opposed to the mid-plane sampled case.

Figure 12 presents the results for the low concentration case, sampled at the mid-plane. We observe less pronounced oscillations in all cases, with a simple exponential decay at the longest range for all correlation types. Similar to the higher concentration case sampled at the walls, Figure 13 presents a more drastic shift from the neutral wall behaviour. For all results at the low concentration case we observe no indication of a frozen state.

Charge-charge and density-density correlations for sRPM(ϕ_n)

To explicitly study the charge-charge and density-density correlations, we computed the corresponding total correlation functions via [7]

$$h_{cc} = \frac{1}{4}(h_{++} + h_{--} - 2h_{+-}) \quad (4)$$

$$h_{nn} = \frac{1}{4}(h_{++} + h_{--} + 2h_{+-}), \quad (5)$$

for all slit separations, at both concentrations (0.13 and 3.4 M) sampled both at the mid plane and the walls. For brevity, the explicit $\rho = \sqrt{x^2 + y^2}$ dependence is omitted. One can easily observe that

$$h_{mean} \equiv \frac{h_{++} + h_{--}}{2} = h_{cc} + h_{nn}. \quad (6)$$

Note, for a RPM in the bulk, i.e., with equal number of cations and anions, $h_{mean} \equiv h_{++} = h_{--}$. Because of the charged walls in our systems leading to a ion number imbalance (to ensure electroneutrality), the short ranged behaviour of the total correlation functions differs slightly, hence the need to formally use the mean like-charge total correlation function. For all intensive purposes, h_{mean} should be treated as a 'system behaviour' correlation function describing the structure of the fluid.

Figures 14, 15, 16, and 17 present the charge- and density- correlations for both the high and low concentration cases, sampled at the walls and mid-plane. On Figure 14 we can observe how density-density correlations begin to dominate the behaviour of the system as we increase the surface separation. Furthermore, we observe how the density-density correlation length increases with increasing surface separation (note the slope on subplot (c)). This effect is less pronounced at the walls, Figure 15, due to poorer statistics.

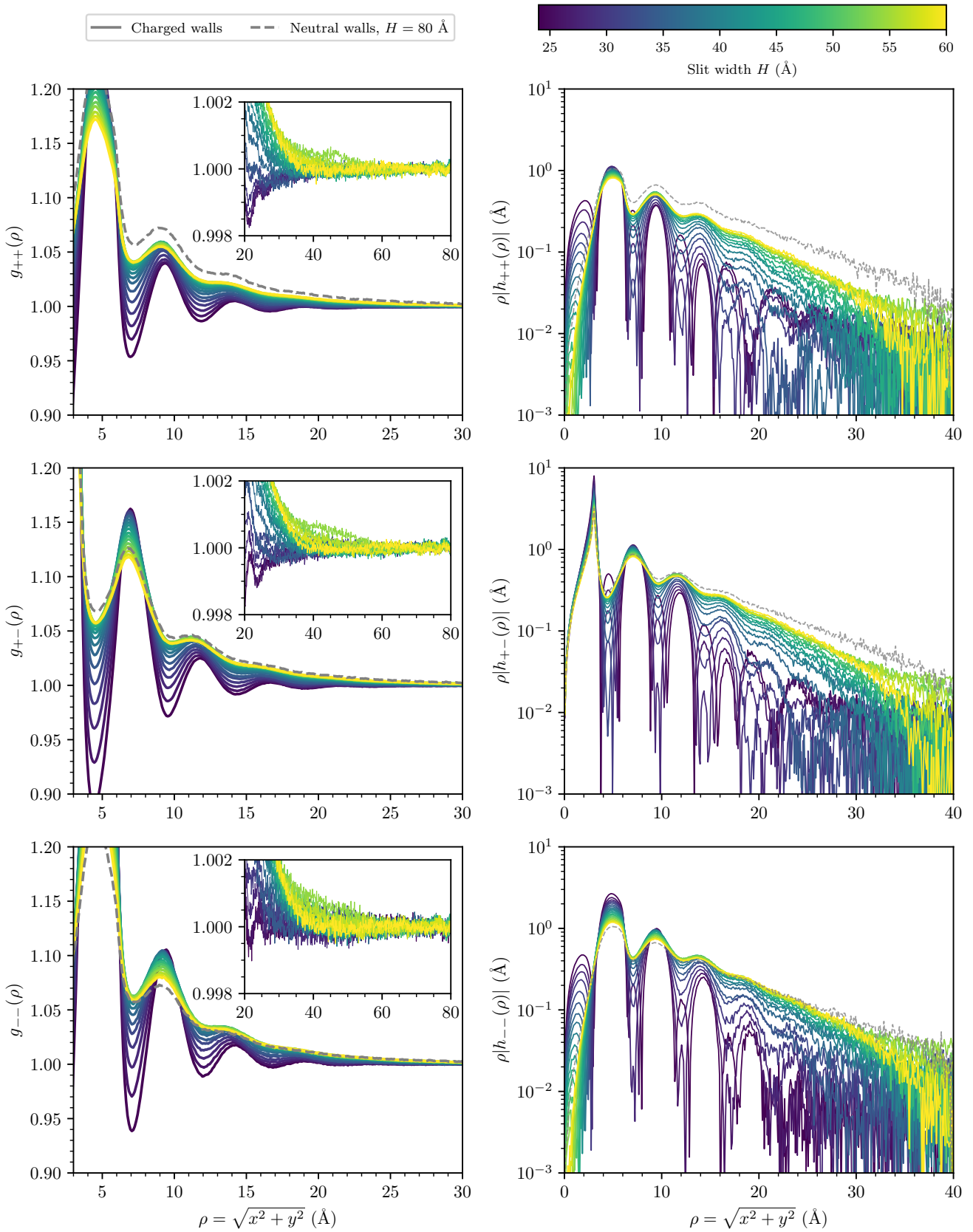


FIG. 10: 2D pair correlation functions, sampled at the mid-plane, for the ≈ 3.4 M sRPM(ϕ_n) system. The top row depicts the $++$ species resolved correlations, the middle $+ -$, and the lowest $--$. The first column presents the pair correlation functions, $g_{\mu\nu}(\rho)$, and the second the total correlation functions, $h_{\mu\nu}(\rho) = g_{\mu\nu}(\rho) - 1$, via an asymptotic analysis type of plot, $\rho|h_{\mu\nu}(\rho)|$. Colour denotes the slit width used in the simulations. The dashed line presents the results for the slit with neutral walls at a slit width of 80\AA .

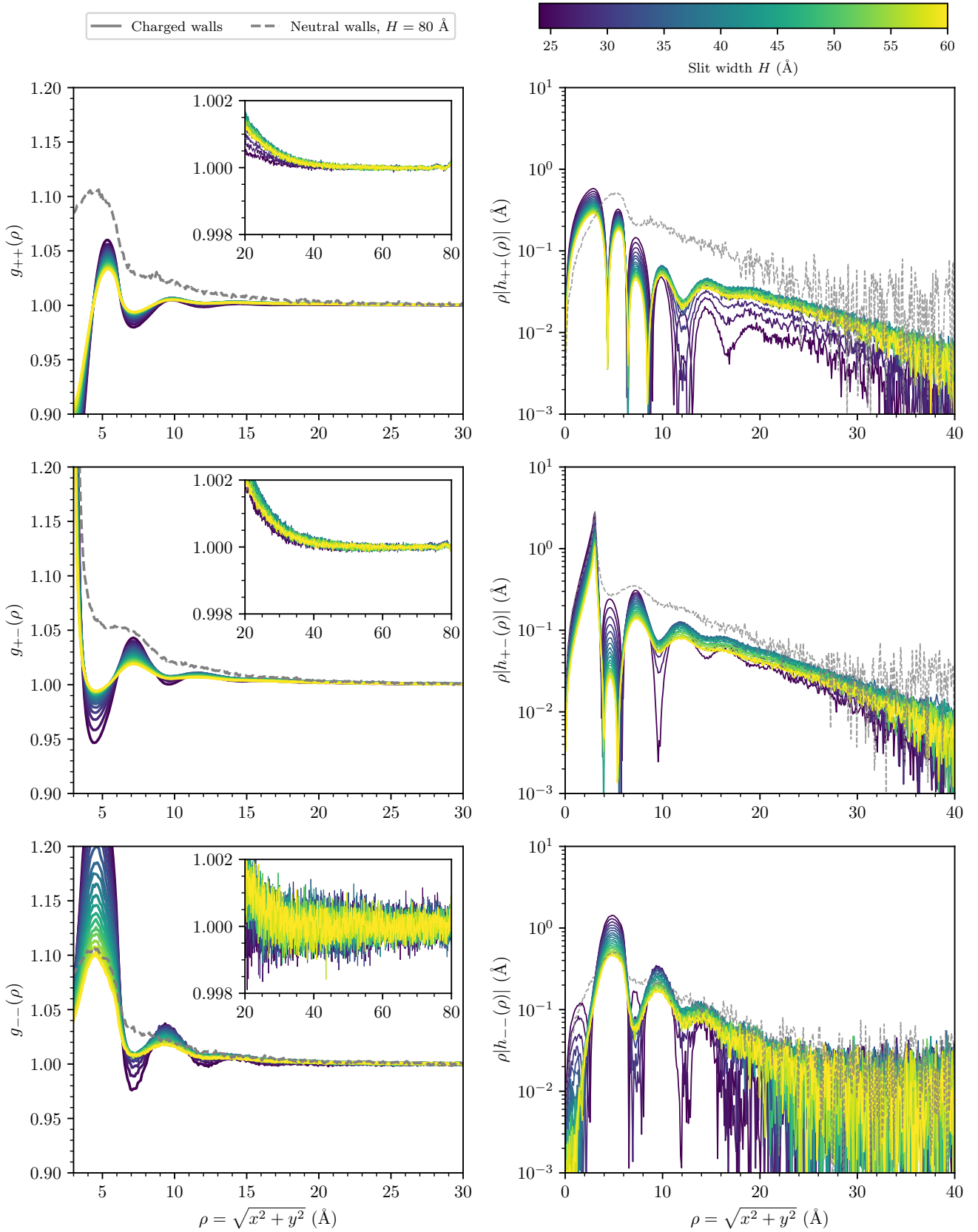


FIG. 11: 2D pair correlation functions, sampled at the walls, for the ≈ 3.4 M sRPM(ϕ_n) system. The top row depicts the $++$ species resolved correlations, the middle $+ -$, and the lowest $--$. The first column presents the pair correlation functions, $g_{\mu\nu}(\rho)$, and the second the total correlation functions, $h_{\mu\nu}(\rho) = g_{\mu\nu}(\rho) - 1$, via an asymptotic analysis type of plot, $\rho|h_{\mu\nu}(\rho)|$. Colour denotes the slit width used in the simulations. The dashed line presents the results for the slit with neutral walls at a slit width of 80 \AA .

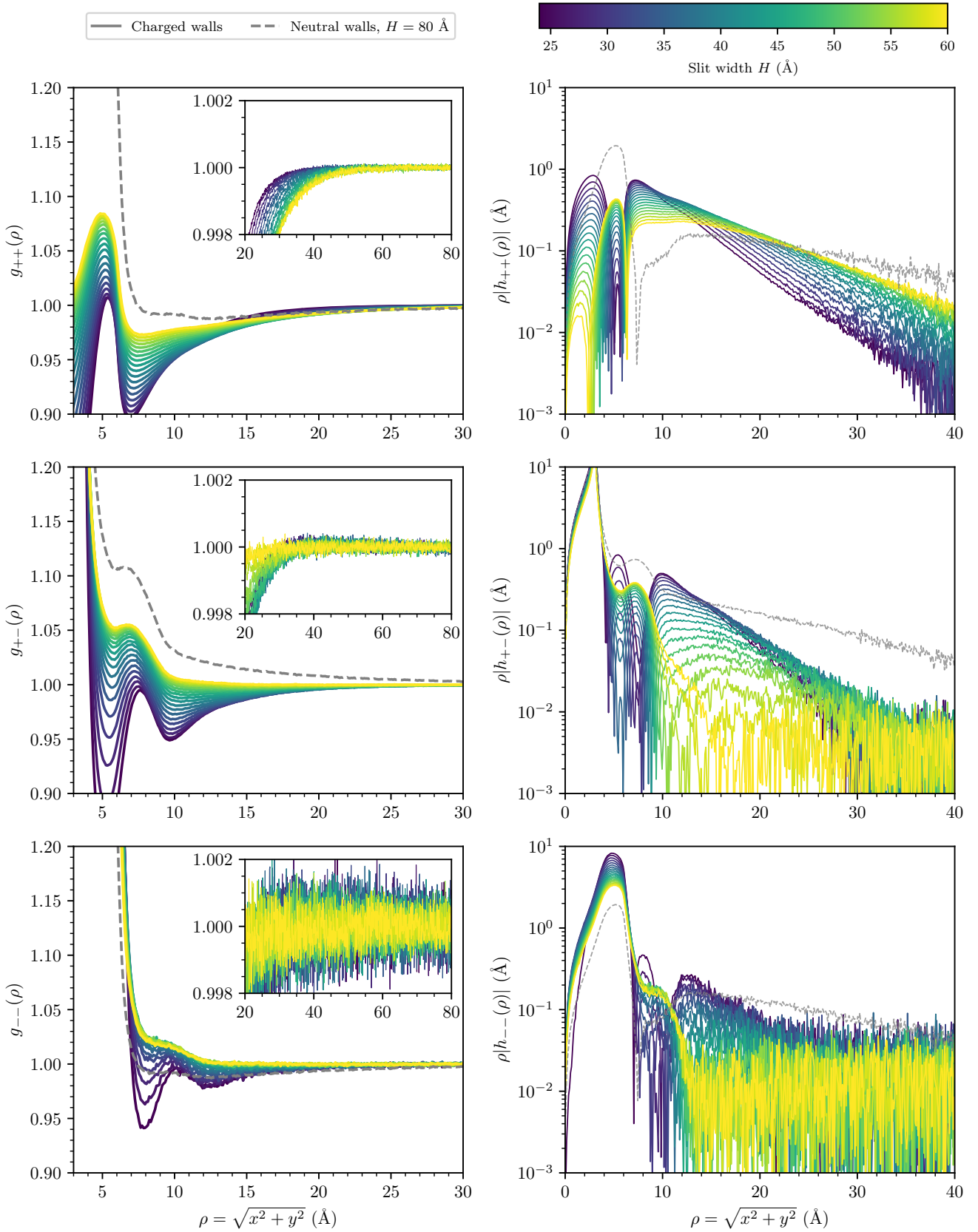


FIG. 12: 2D pair correlation functions, sampled at the mid-plane, for the ≈ 0.13 M sRPM(ϕ_n) system. The top row depicts the ++ species resolved correlations, the middle +-, and the lowest --. The first column presents the pair correlation functions, $g_{\mu\nu}(\rho)$, and the second the total correlation functions, $h_{\mu\nu}(\rho) = g_{\mu\nu}(\rho) - 1$, via an asymptotic analysis type of plot, $\rho|h_{\mu\nu}(\rho)|$. Colour denotes the slit width used in the simulations. The dashed line presents the results for the slit with neutral walls at a slit width of 80 Å.

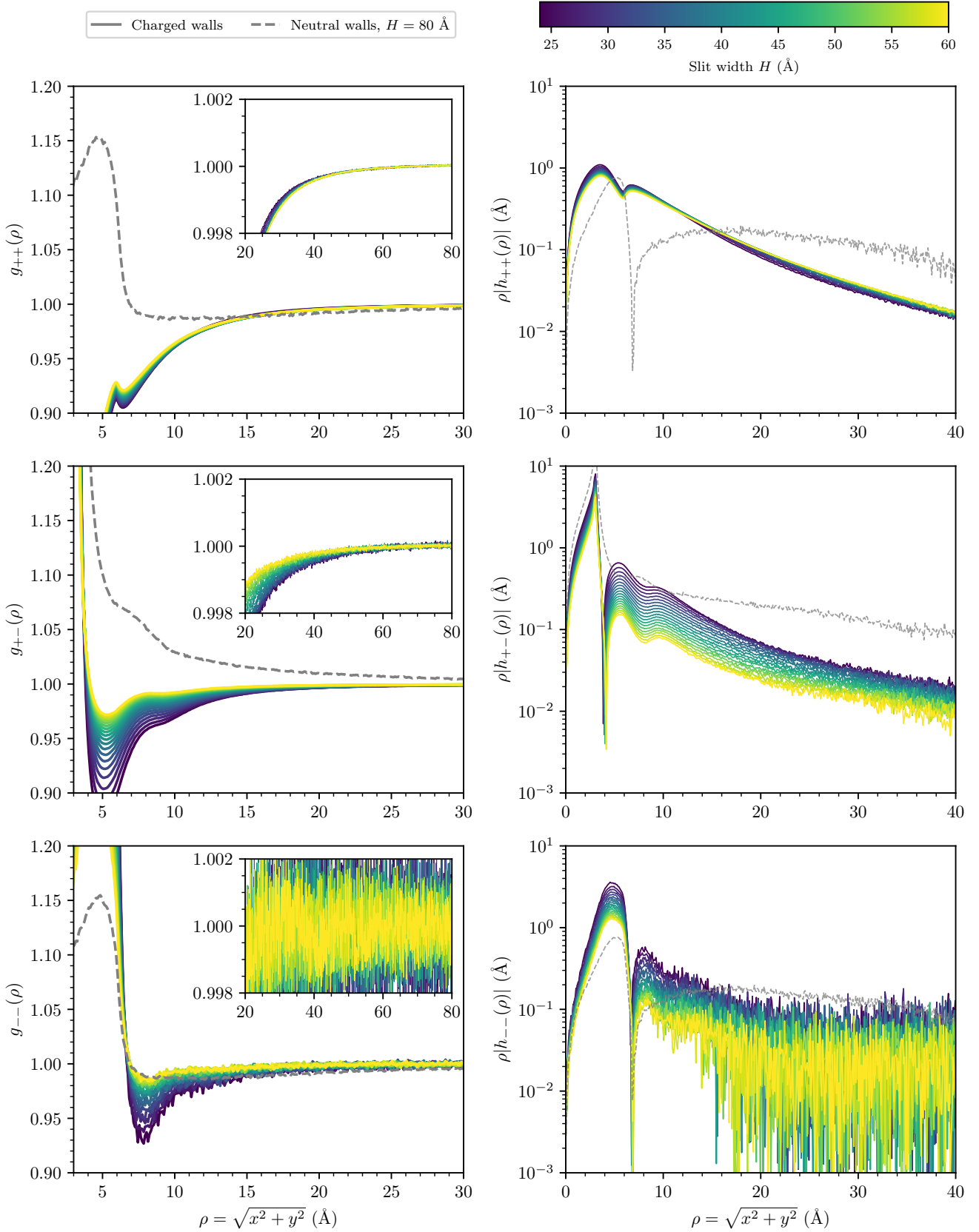


FIG. 13: 2D pair correlation functions, sampled at the walls, for the ≈ 0.13 M sRPM(ϕ_n) system. The top row depicts the ++ species resolved correlations, the middle +-, and the lowest --. The first column presents the pair correlation functions, $g_{\mu\nu}(\rho)$, and the second the total correlation functions, $h_{\mu\nu}(\rho) = g_{\mu\nu}(\rho) - 1$, via an asymptotic analysis type of plot, $\rho|h_{\mu\nu}(\rho)|$. Colour denotes the slit width used in the simulations. The dashed line presents the results for the slit with neutral walls at a slit width of 80 \AA .

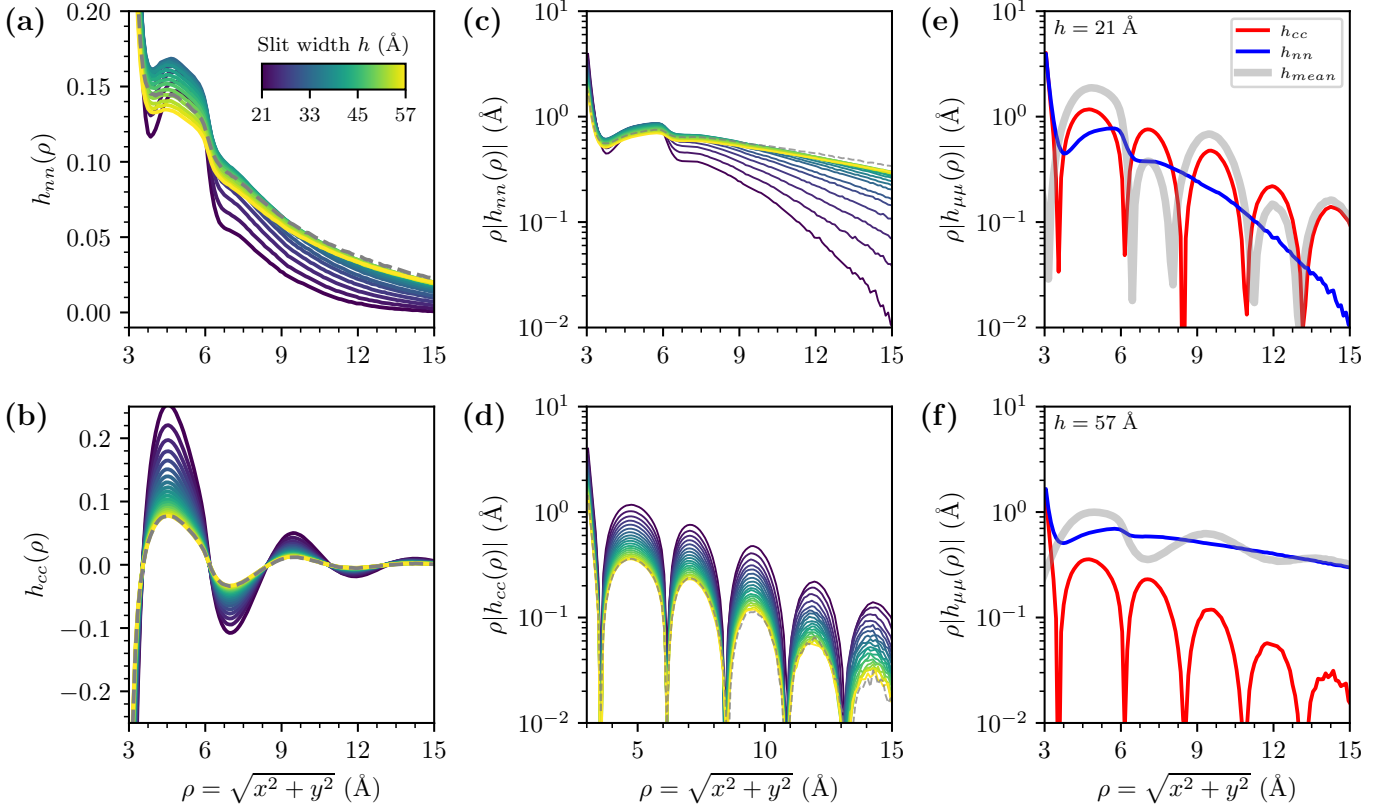


FIG. 14: Charge-charge and density-density total correlation functions, sampled at the mid-plane, for the ≈ 3.4 M sRPM(ϕ_n) system. The gradient denotes the slit width used, with $h = 21$ Å for the purple and $h = 57$ Å for the yellow. The dashed line indicates the results for the neutral walls at $h = 77$ Å. (a) charge-charge and (b) density-density total correlation functions on a linear scale. (c) and (d) present the asymptotic analysis plot on a log scale. (e) presents the asymptotic analysis plot for the smallest surface separation and (f) for the largest slit width.

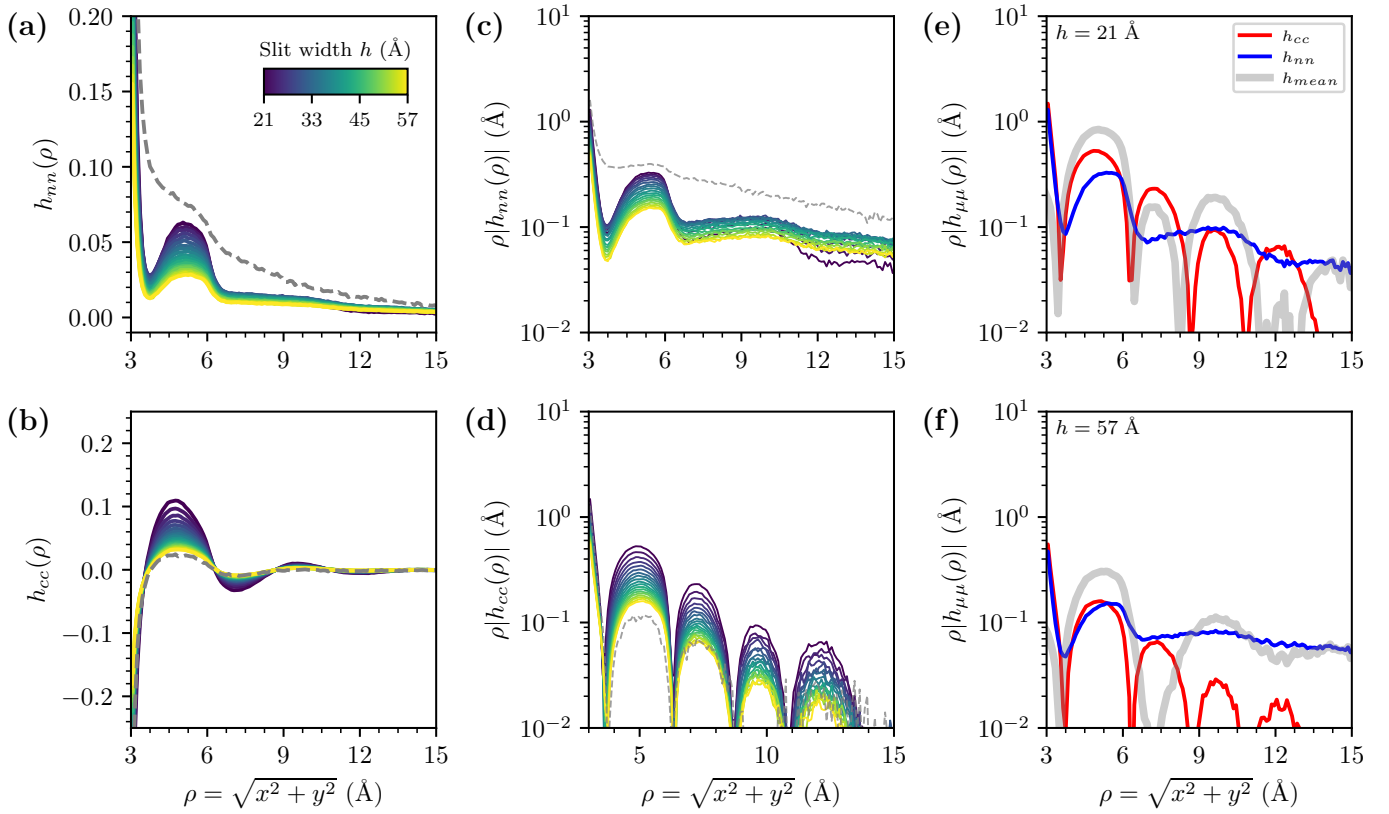


FIG. 15: Same as Figure 14, but sampled at the walls for the ≈ 3.4 M sRPM(ϕ_n) system.

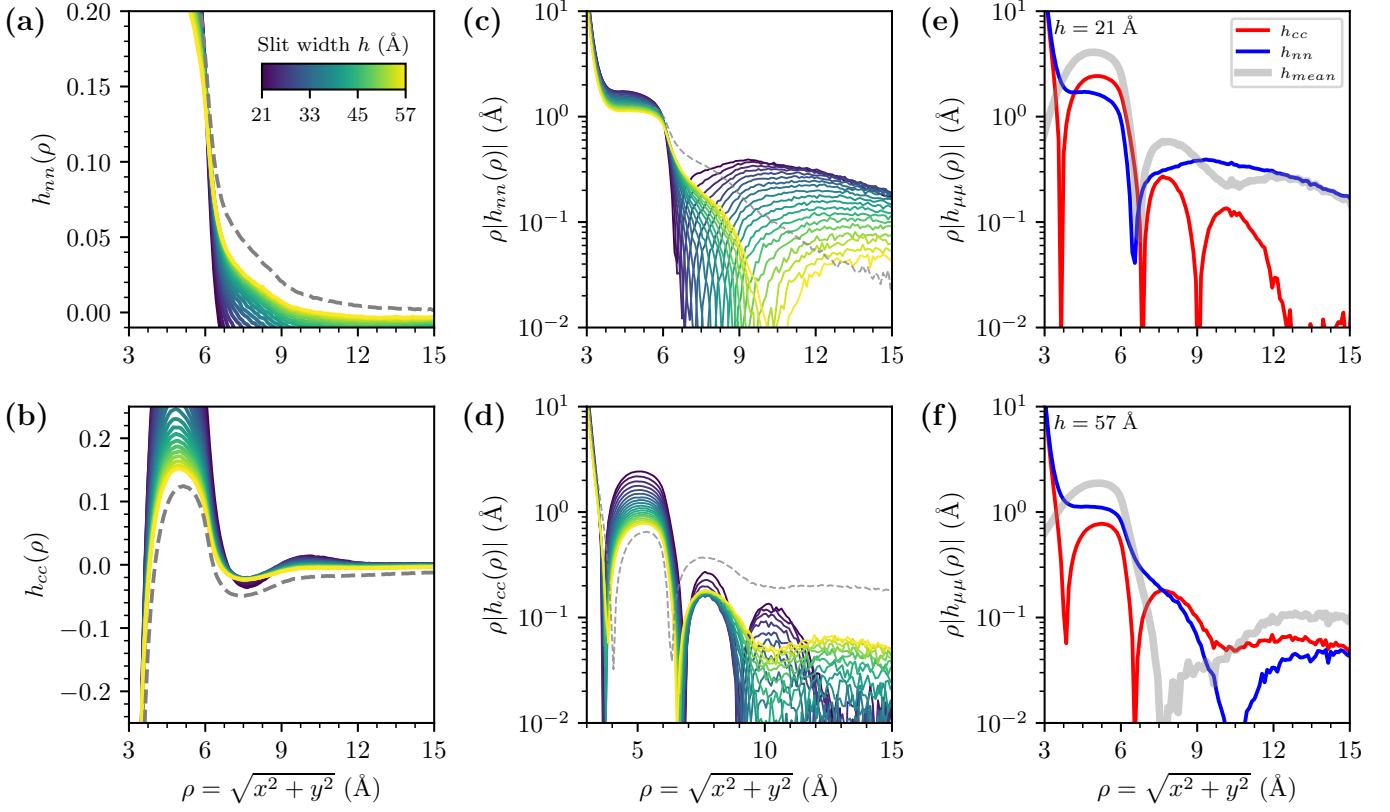


FIG. 16: Same as Figure 14, but sampled at the mid-plane for the ≈ 0.13 M sRPM(ϕ_n) system.

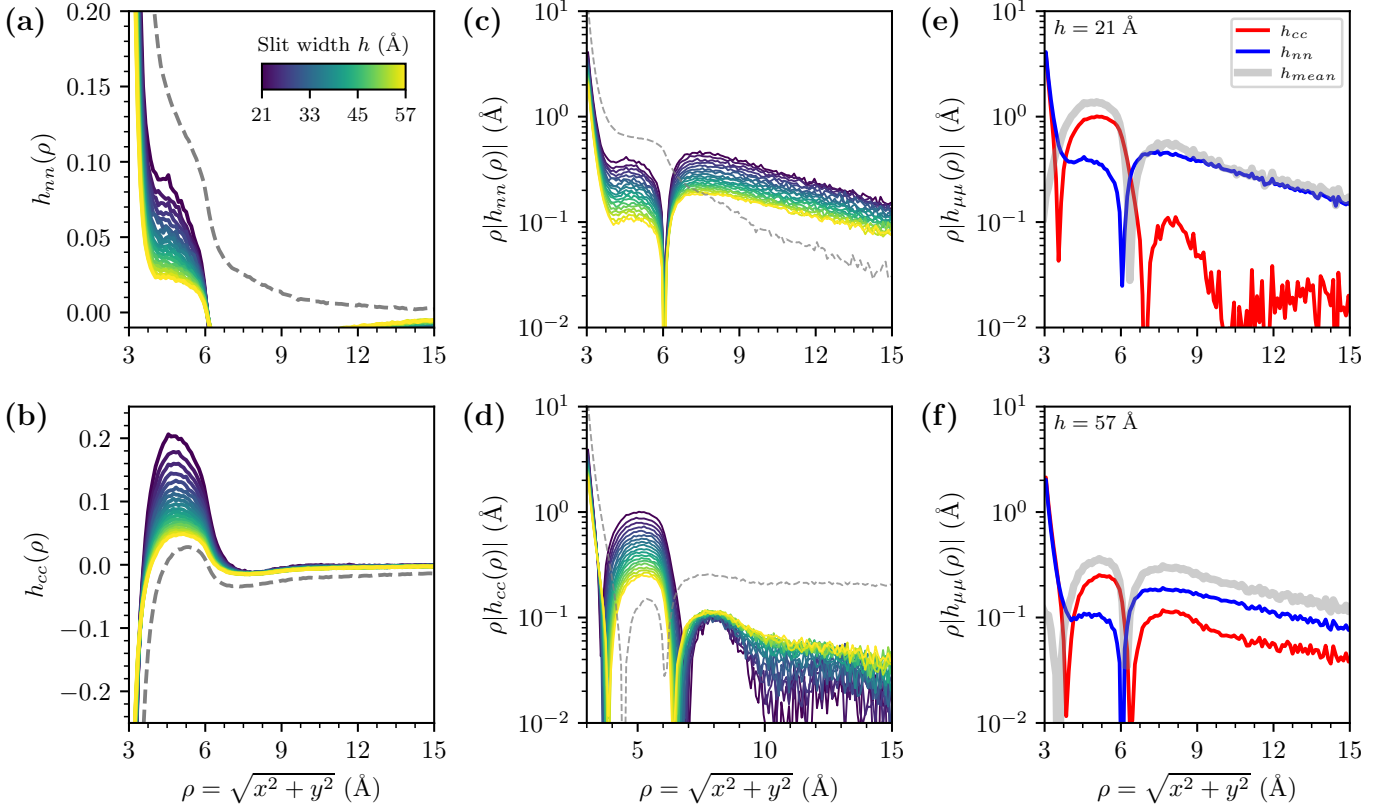


FIG. 17: Same as Figure 14, but sampled at the walls for the ≈ 0.13 M sRPM(ϕ_n) system.

Figure 18 presents a comparison of correlation functions at the smallest and largest surface separations with the bulk correlation functions for the low concentration $c \approx 0.13$ M system. We can see that the charged walls induce a small difference in the behaviour of the correlation functions, differences on Figure 18(b-c). The difference between a system with neutral walls and the bulk is in the amplitude (downwards shift on the y -axis), with other correlation lengths being almost identical.

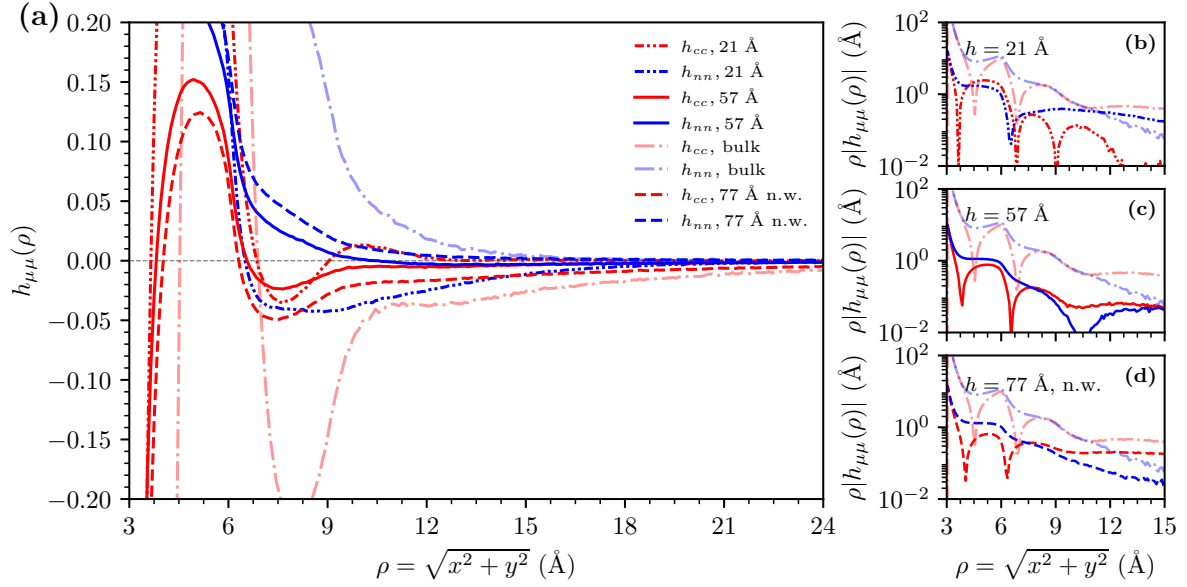
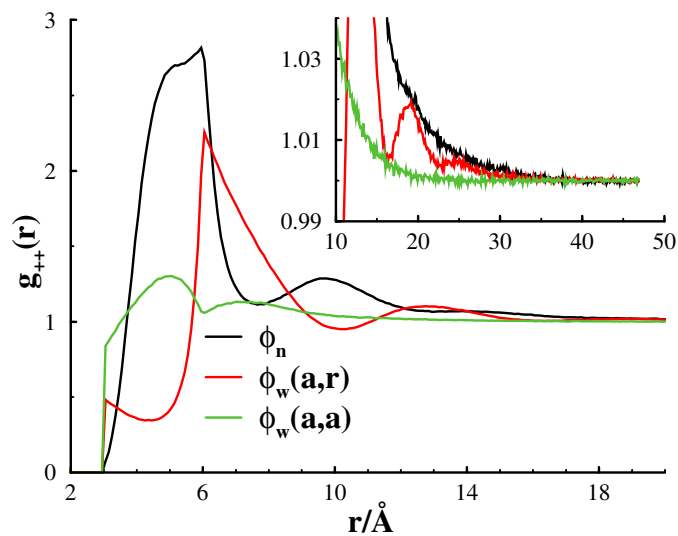


FIG. 18: Comparisons of correlation functions obtained for the $c \approx 0.13$ M sRPM(ϕ_n) system at the mid plane for $h = 21$ Å , $h = 57$ Å charged wall systems, as well as the $h = 77$ Å neutral wall (n.w.) system, with bulk correlation functions. For the bulk, all correlation functions have a standard radial dependence i.e. $h_{\mu\mu} \equiv f(r)$.

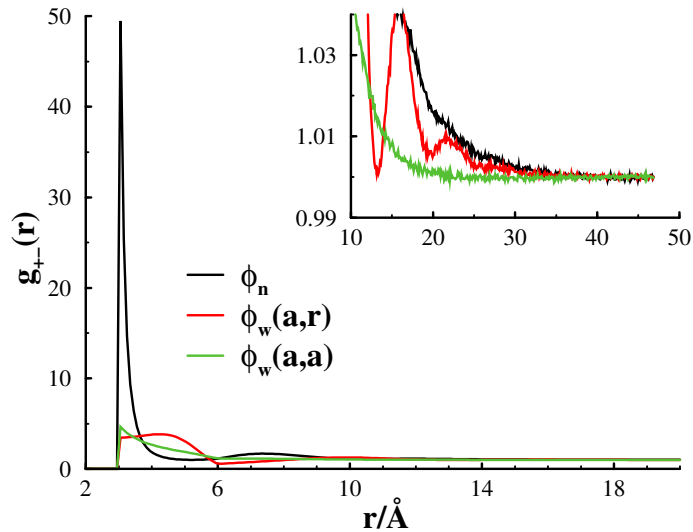
Structural comparison, using different sPMF:s in a concentrated bulk solution

The explicit comparison between the bulk structure obtained with different choices of the sPMF, is presented on Figure 19. Firstly, we can observe higher 'contact' values at $r = 3 \text{ \AA}$ for the ϕ_n ("narrow") sPMF on Figure 19(b). This corroborates with the higher probability of finding dimers, according to the cluster analysis presented in the main article. Furthermore, we can observe a higher amplitude for the unlike-attractive, like-repulsive "wide" sPMF $\phi_w(a, r)$ when compared to the purely attractive $\phi_w(a, a)$. This tells us that the presence of a short-ranged enhanced repulsion between like charges promotes configurations with more "expanded" clusters, whereas an overall attractive sPMF generates more compact clusters. Applying $\phi_w(a, r)$ or ϕ_n , we observe a long-ranged decay of g_{++} and g_{+-} following a similar pattern for the same sPMF, irrespective of the actual identity of the radial distribution function, i.e., $g_{++} \approx g_{+-}$ for $r \rightarrow \infty$. This is the hallmark of long-ranged decay in clustering systems [6].

-
- [1] A. R. Crothers, C. Li, and C. Radke, *Advances in Colloid and Interface Science* **288**, 102335 (2021).
 - [2] G. M. Torrie and J. P. Valleau, *J. Chem. Phys.* **73**, 5807 (1980).
 - [3] J. Forsman, D. Ribar, and C. E. Woodward, *Physical Chemistry Chemical Physics* **26**, 19921–19933 (2024).
 - [4] S. Stenberg and J. Forsman, *Langmuir* **37**, 14360 (2021).
 - [5] A. M. Smith, A. A. Lee, and S. Perkin, *J. Phys. Chem. Lett.* **7**, 2157 (2016).
 - [6] D. Ribar, C. E. Woodward, S. Nordholm, and J. Forsman, *J. Phys.Chem. Lett.* **15**, 8326–8333 (2024).
 - [7] R. Leote de Carvalho and R. Evans, *Mol. Phys.* **83**, 619–654 (1994).



(a)



(b)

FIG. 19: Comparing radial distribution functions, using various sPMF:s, as described by the legends. The inserts present the long range decay on a linear scale. The salt concentrations are all in the regime 1.6-2M.

- (a) Radial distribution functions between like charges ($++$) for various sPMF. (b) Radial distribution functions between unlike charges ($+-$) for various sPMF.